Photocopy & Use Authorization

In presenting this thesis in partial fulfillment of the requirements for an advanced degree at Idaho State University, I agree that the Library shall make it freely available for inspection. I further state that permission for extensive copying of my thesis for scholarly purposes may be granted by the Dean of the Graduate School, Dean of my academic division, or by the University Librarian. It is understood that any copying or publication of this thesis for financial gain shall not be allowed without my written permission.

Signature _____

Date _____

Microstructure Characterization and Thermal Stability of Equal Channel Angular Pressing Processed Grade 91 Stainless Steel

By

Ryan Carnahan

A thesis

Submitted in partial fulfillment

Of the requirements for the degree of

Master of Science in the Department of Nuclear Engineering

Idaho State University

Summer 2018

To the Graduate Faculty:

The members of the committee appointed to examine the thesis of Ryan Carnahan find it satisfactory and recommend that it be accepted.

_____

Mary Lou Dunzik-Gougar
Committee Chair

_____

Haiming Wen
Major Advisor, Committee Member

_____

Cheng Sun
Major Advisor, Committee Member

_____

Rene Rodriguez
Graduate Faculty Representative

Acknowledgements

The credit of this work goes to the guidance and leadership of Dr. Cheng Sun and Prof. Haiming Wen, the experimental and analytical contributions of PhD candidate Malwina Wilding, the technical support and expertise of the lab team and safety officers at the Center for Advanced Energy Studies (CAES), and the ever-present love and support of my wife Tashara, who's faith, comfort, and encouragement pushed me through the times of anxious self-doubting and who gave me the strength to keep facing the unknown.

This research work is financially supported through the INL's Laborotory Directed Research and Development (LDRD) program under DOE Operations Office Contract DE-AC07-051D14517. We thank Prof. Haiming Wen and Prof. R. Z. Valiev for providing the samples in this study.

Table of Contents

List of Figures

List of Tables

Microstructure characterization and thermal stability of equal channel angular pressing processed Grade 91 stainless steel

Thesis Abstract--Idaho State University (2018)

Abstract

This work describes the microstructural characterization of Grade 91 stainless steel pre/post equal channel angular pressing (ECAP). Results are intended to be used as a baseline comparison for future neutron irradiation experiments to be performed in ATR. Ultra-fine grained Grade 91 is a potential structural material for advanced fast reactors. These samples are also ex-situ thermally annealed at 600, 700, and 800° C, and compared with in-situ thermal annealing at 700° C, a process which has never been done before with ECAP Grade 91. ASTAR is also performed for the first time on this material to obtain phase and orientation maps of ultra-fine precipitates (mostly Cr and V carbides). Significant grain and precipitate refinement was observed after ECAP processing. The bulk of dislocation networks recover in the first 15 minutes of annealing time. Also, the design and operation of a new experimental ECAP facility are described.

Key words: Equal channel angular pressing (ECAP); Grade 91 stainless steel; In-situ thermal annealing; ASTAR

1.0 Introduction

Nuclear power is one of the densest, most independent forms of energy yet discovered by man. Unlike hydroelectric, solar, and wind, nuclear can operate independent of geographic location and weather. Unlike coal, it does not require frequent replenishing of large amounts of fuel and does not emit carbon pollution. Space exploration where light payloads are mission critical, remote power operations such as mining where infrastructure is non-existent and the year's seasons partially restrict fuel deliveries, large cities and small communities where human populations are concerned with pollution levels and maintaining base-load power demands, all these can benefit from the consistency, reliability, and independence that nuclear power brings to the table.

To become more economically competitive and more socio-politically accepted, to heal the fear instilled by nuclear related accidents of the past, this still relatively new technology needs to evolve. Reactors capable of 80 years of operation over the current 60 year terms would make reactor technology more appealing to investors who would get higher returns per build. Smaller, more modular designs would be cheaper and potentially easier to manufacture, build, and install, and bring nuclear to more widespread applications. New, more efficient designs with sophisticated redundant and passive safety systems eliminate the catastrophizing potential of nuclear accidents. Higher temperatures and greater neutron fluxes could improve efficiency and fuel economy and minimize waste. But the one factor upon which all these next generation reactor concepts hinge is the physical limitations of the materials available to build them. Structural materials need to exhibit sufficient strength, ductility, thermal conductivity, formability and weldability, corrosion resistance, and appropriately low neutron cross-sections,

all while performing at higher temperatures and greater radiation fluences [Murty et al., 2013]. How can we ensure that potential materials maintain these desirable properties in an irradiated environment long term? This work will explore one of the most promising materials for generation IV reactors, Grade 91 stainless steel (SS), and the enhanced properties it exhibits after being mechanically processed through equal channel angular pressing (ECAP). This material, combined with ECAP, may prove to play a critical role in advancing this amazing technology into a new era of clean energy.

1.1 Background

Ferritic/martensitic (F/M) stainless steels and ultra-fine grained (UFG) materials have been a major area of interest for the past several years and are now becoming the most prominent topics of discussion in relation to next generation reactor materials. To give context to this interest and to better understand the purpose and intent of this research, it is instructive to consider the effects of neutron irradiation on materials and how the environment of next generation reactors differs from the traditional reactors of today.

1.1.1 Material Requirements for the Reactors of Tomorrow

Neutron irradiation causes neutron damage to materials through collision mechanisms, displacing atoms from lattice sites to create point defects such as voids and interstitials that can lead to shifts in overall microstructure and ultimately effect mechanical/chemical properties of materials [Chen, 2013]. Quantified as displacements per atom (dpa), this damage can lead to hardening due to formation of dislocation loops and precipitation of secondary phases, corrosion cracking caused by irradiation-induced segregation, swelling caused by transmutation of material constituent elements, and evolutions in tensile strength, creep resistance, ductile-to-brittle

transition temperature, and fatigue behaviors. On top of these irradiation effects, next generation reactor designers are leaning toward fast spectrum fluxes and elevated temperatures, both of which could exacerbate these effects [Murty et al., 2008]. Table 1 provides a list of next generation reactor types and the neutron spectrums and operational temperature ranges being considered. Current estimates show that materials for next generation reactors will need to sustain damage on the order of >300 dpa over their operational lifetime while incurring thermal stresses in a corrosive environment [Muralidhar et al., 2013].

Table 1: Generation IV reactor types [Murty et al., 2008]

Reactor system	Coolant	Neutron spectrum	Core outlet temp. (°C)
Gas-cooled fast reactor (GFR)	Gas (e.g. He)	Fast	~850
Lead-cooled reactor (LFR)	Liquid metal (e.g. Pb, Pb-Bi)	Fast	550-800
Molten salt reactor (MSR)	Molten salt (F salts)	Thermal	700-800
Sodium-cooled fast reactor (SFR)	Liquid metal (Na)	Fast	~550
Super critical water-cooled reactor (SCWR)	Water	Thermal/Fast	350-620
Very high temperature reactor (VHTR)	Gas (e.g. He)	Thermal	>900

1.1.2 F/M Stainless Steels

F/M stainless steels, originally developed around 60 years ago for use in fossil fuel plants, now hold a lot of promise in nuclear applications and have stirred up a renewed interest among material developers as having the potential for maintaining desirable properties under these high flux, high temperature conditions. Research has shown that F/M steels have reduced activation over other steels, allowing for shallower burial depths of replaced/decommissioned components [Murty et al., 2008]. As for in-core operation performance, F/M steels, particularly those containing 9-12 wt.% Cr, also exhibit low thermal expansion, high thermal conductivity, and better resistance to irradiation-induced swelling, irradiation-assisted stress corrosion cracking, and is less subject to transmutation than austenitic stainless steels [Bachhav et al., 2014; Song et

al., 2016]. Figure 1 demonstrates the superior swelling resistance of F/M steels, being orders of magnitude lower than austenitic steel options.

Grade 91, a 9 wt.% Cr, 1 wt.% Mo blend F/M steel, has specifically shown resistance to corrosion from liquid metal coolants, and has desirable ductility as well [Song et al., 2013]. Because of its long history, Grade 91 is already fabricated on a large scale and readily available, only adding to its appeal for cladding and other structural reactor applications. It is for these reasons that Grade 91 was selected as the focus of this work.

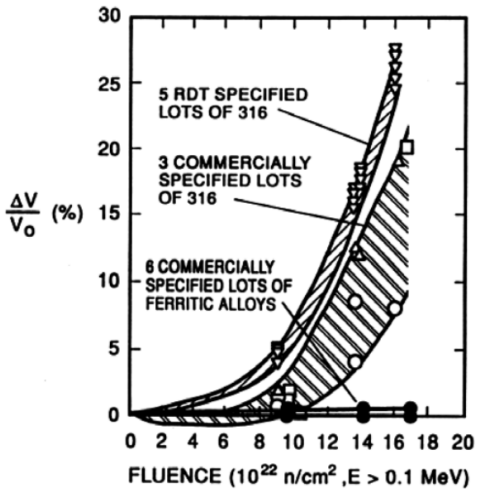

Figure 6: Comparison of swelling behavior of commercial ferritic/martensitic steels with commercial type 316 stainless steel at 420°C [Klueh et al., 2007]

1.1.3 Ultra-Fine Grained Materials

As promising as F/M stainless steels are on their own, researchers have found that refining the grain structure into the ultra-fine grain (UFG) regime (100-1000 nm average grain diameters) further enhances the irradiation resistance of some materials. For example, C. Sun et al. found that nano-engineering of grains led to reduced swelling of irradiated 304L SS to the effect of nearly an order of magnitude difference from larger grained specimens [Sun et al., 2015]. M.

Song et al. reported lower defect density, three times less swelling, and shallower peak damage penetration depth in UFG T91 (prepared by normalization and tempering for 0.5h each at 1038 and 760° C, respectively, with air cooling between, followed by two ECAP passes of route B extruded at 300° C) as compared to coarse grain (CG) T91 when exposed to Fe ion irradiation [Song et al., 2014]. Z.Q. Fan et al. have shown that these results are due to the large volume fraction of grain boundaries (GB) which act as sinks for neutron irradiation-generated defects in UFG material compared to their CG counterparts [Fan et al., 2013; Yu et al., 2012]. These results have led to several additional studies on the thermal and long term irradiation stability of these refined grain structures to determine whether the exhibited characteristics would survive the harsh environments of high temperature fast reactors.

1.1.4 Severe Plastic Deformation

Up to this point, ultra-fine grained Grade 91 has risen as a strong competitor for next generation cladding and structural material. But, the next big question to answer is whether such an engineered microstructure can be fabricated on a large enough scale for production to move forward. The two general approaches for fabricating nano- or ultra-fine grained materials are as follows: 1. Bottom-up techniques, where small particles are ground, refined, and consolidated into a bulk sample and 2. Top-down techniques where bulk billets are subjected to severe plastic deformation to refine existing grains. Bottom-up techniques, such as ball milling, gas condensation, and other methods have been found to readily introduce contaminants, owing to the large surface area of powders, and lend themselves to the formation of undesirable porosity, owing to insufficient compaction and poor bonding. This porosity effectively decreases the elastic constants, strength, and ductility of the resultant material [Meyers et al., 2006; Valiev et al., 2000]. There are currently two top-down techniques widely used, high pressure torsion

(HPT) and equal channel angular pressing (ECAP) [Meyers et al., 2006]. Both can produce fully dense (non-porous) material, however HPT does not currently have a practical means of being scaled up for producing production level billets [Valiev et al., 2000]. ECAP is not only scalable but also allows for multiple slip systems to be activated by varying the insertion orientation of samples through multiple passes, resulting in a more complete three-dimensional processing and exceptionally high strains [Huang et al., 2006; Muralidhar et al., 2013; Valiev et al., 2006]. Equal channel angular pressing, with its simplicity, versatility, and scalability, has become the most prominent method of severe plastic deformation for grain refinement, and thus ECAP processed Grade 91 will be the specific focus of this work.

1.1.5 ECAP Processed Grade 91

With the promising results of ECAP for grain refinement and the naturally exceptional properties of Grade 91 SS, much research has been performed on ECAP Grade 91, both through various ECAP parameters post-ECAP annealing, and even some heavy ion irradiation tests have been performed [Fan et al., 2013; Hao et al., 2014; Jones et al., 1991; Maier et al., 2013; Shrestha et al., 2015; Song et al., 2013; Song et al., 2014; Song et al., 2016]. Microstructural characterization of ECAP Grade 91 has already been performed using several techniques and has revealed the presence of various precipitate structures in Grade 91 prior to ECAP processing [Klueh et al., 2007; Song et al., 2013]. These precipitates can have a significant effect on the thermal stability of the material, acting as obstacles to dislocation motion and grain growth mechanisms at high temperatures, effectively raising the activation energy for grain growth and prolonging the life of the desirable characteristics of UFG Grade 91 [Maier et al., 2013]. This carbide strengthening effect may hold the key to Grade 91's success as a structural material in future reactors.

To characterize the effect of ECAP processing on these important precipitates, electron backscatter diffraction (EBSD), a technique for determining grain size/phase distributions and creating orientation maps, has been used to characterize the microstructure of ECAP-processed Grade 91. However, with minimum step sizes on the order of ~150 nm, it is possible that the distribution of finer precipitates may not have been fully characterized in previous work [Maier et al., 2013]. A relatively new method of characterization known as ASTAR, which uses a transmission electron microscope (TEM) based beam precession technique to acquire diffraction spots for phase and orientation mapping but at much higher spatial resolutions (step sizes as small as 1-10 nm), offers the potential to map the size and distribution of precipitates more accurately. Similarly, ex-situ thermal annealing has been performed and post annealing observations made, but an in-situ annealing examination of this material, which could prove insightful into the specific mechanisms at work during annealing of ECAP-processed Grade 91, has yet to be conducted.

1.2 Objective

This body of research constitutes the initial phase of a much larger research project in which several candidate materials for future reactors, including pre/post-ECAP processed Grade 91, will be irradiated in ATR to 3 and 5 dpa. The goal and intent of this work is to create a base-line characterization of pre/post-ECAP processed Grade 91 for comparison against future neutron irradiated specimens of the same make. In part, this research will verify results obtained by other researchers on the microstructure of Grade 91, but will also introduce characterization techniques new to the study of Grade 91, namely ASTAR and in-situ thermal annealing. These techniques are aimed to generate higher resolution phase/orientation maps of bulk material than what has previously been obtained and to gain insight into the mechanisms involved in microstructural

evolution during thermal annealing. Details of the construction and operation of an Idaho National Labs based ECAP facility are also discussed, which will aid in the production of more ECAP samples in the future and be incorporated into the National Science User Facilities (NSUF) network.

2.0 Literature Review

2.1 ECAP Parameters

There are various parameters unique to ECAP processing that each play a role in the effective grain refinement and texturing of samples processed with this technique. Here, an overview of the geometric parameters will be presented, followed by a discussion of why the specific parameters for the samples processed in this work were selected.

Figure 2 gives a simple schematic of an ECAP set up. ECAP is constructed of a die with an

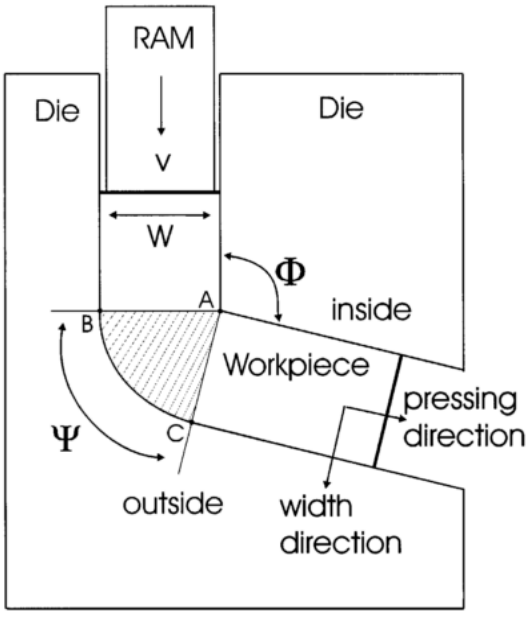

Figure 7: Schematic illustration of the ECAP process showing the die channel angle geometry. Pressing direction, width direction and thickness direction denote three perpendicular directions with reference to the work piece [Kim, 2001]

abrupt bend. This bend has an inside angle (commonly denoted as Φ in literature) and an outside angle (commonly denoted as ψ). Other parameters that can be altered are pressing route, number of passes, pressing rate, and pressing temperature.

The effects of Φ, ψ, and number of passes on equivalent strain induced on an extruded billet through ECAP is estimated as:

$$\varepsilon = \frac{N}{\sqrt{3}}\left[\cot\left(\frac{\phi}{2}+\frac{\Psi}{2}\right)+\Psi\csc\left(\frac{\phi}{2}+\frac{\Psi}{2}\right)\right]$$

[Shin et al., 2003; Valiev et al., 2006]. Figure 3 plots the estimated equivalent strain equation through various Φ and ψ values through a single pass. Ruslan Z. Valiev et al. have shown that the outside angle, ψ, contributes largely to the inhomogeneity of pressed samples as large angles correspond to a spreading of the shear zone [Valiev et al., 2006]. This inhomogeneity can be explained by the faster flow of material through the outer angle compared to the flow of material through the inner angle [Kim, 2001]. However, these effects can be minimized by using a larger

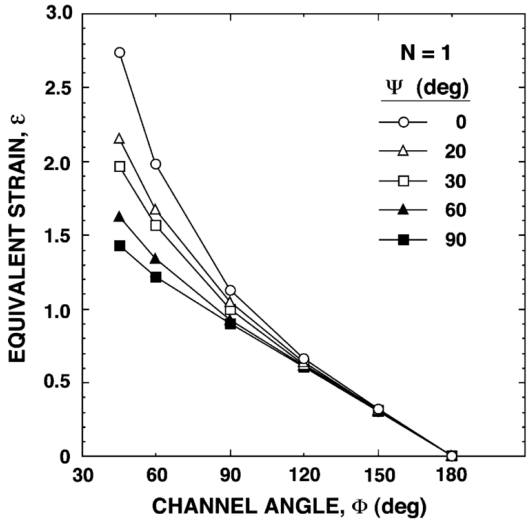

Figure 8: Variation of equivalent strain, ε, with the channel angle, Φ, over an angular range of Φ from 45° to Kim, 20010° for values of the angle of the arc of curvature, Ψ, from 0° to 90°: the strains are shown for a single pass where N=1 [Valiev et al., 2006]

Φ. The samples prepared for this work were extruded through a die with Φ = 120° to minimize sample cracking by reducing the equivalent strain per pass.

Temperature is another parameter that can be adjusted during ECAP processing. The extrusion process for this study was conducted at elevated temperatures, around 300° C. According to M. Song et al., hot-ECAP can refine carbide particles much further than cold or room temperature ECAP processing [Song et al., 2013]. By creating a high density of carbide nano-precipitates through ECAP at elevated temperatures, it is more likely that refined grain structures will be "pinned" into place as precipitates at GBs can inhibit grain growth by acting as barriers to diffusion mechanisms. Nanoscale carbides formed by hot-ECAP are also more thermally stable against coarsening at elevated temperatures, a desirable quality sought after for next generation reactor materials [Song et al., 2013].

There are various routes or modes of sample reinsertion possible with ECAP, each producing unique results by activating different slip planes. Depending on the route selected, certain characteristic texturing may be formed in the material. Of the various routes, route Bc was selected for this work due to its exceptional ability to create homogeneity in all three directions in the shortest number of passes, as compared to other routes [Djavanroodi et al., 2014; Rifai et al., 2014; Valiev et al., 2006]. Figure 4a provides the specific mode of reinsertion characteristic of the Bc route, in which the sample is rotated counterclockwise along the extrusion direction axis between each pass. Figure 4b illustrates the slip planes activated respective to the first 4 passes, after which the sequence of activated slip planes repeats. After the first 4 passes, the microstructure becomes homogeneous and remains so through subsequent passes [Huang et al., 2007]. It has also been shown that route Bc is effective at populating a sample with predominantly high angle grain boundaries (HAGB) after just three passes, which have a higher

dislocation absorption capacity than low angle grain boundaries (LAGB) [Nashith et al., 2014; Song et al., 2013].

In summary, the ECAP processing parameters used in this work are a Bc route through at 120° bend at 300° C. The samples will be subject to six passes to replicate the parameters used by Galina G. Maier et al. to establish a baseline comparison to their annealing work on Grade 91 stainless steel [Maier et al., 2013].

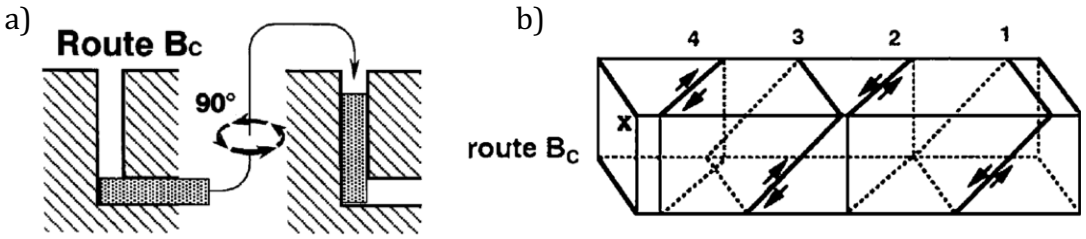

Figure 9: a) Showing ECAP route Bc where a sample is rotated 90° along the pressing direction axis counterclockwise between each successive pass; b) Showing the slip planes activated in the sample through a Bc route. Note slip planes are canceled out in every other pass, resulting in a highly homogeneous structure in the fewest number of passes [Valiev et al., 2006]

2.2 Thermal Annealing

Although in-situ thermal annealing has never been performed on ECAP-processed Grade 91, ex-situ thermal annealing has. To give a valid comparison between the results of this work and work done previously, similar temperatures and durations were used in this work as were used by T. Hao et al., namely 600, 700, and 800° C, which represent the window in which recrystallization initiates and stabilizes [Hao et al., 2014; Maier et al., 2013]. This temperature range also represents the operational temperatures of both fast spectrum gas and lead cooled reactors, as well as SCWRs [Murty et al., 2008].

2.3 Williamson-Hall Approximations from XRD Data

X-ray diffraction (XRD) is a useful technique for determining the phase composition of a material and operates on the principles of Bragg's Law:

$$n\lambda = 2d \sin \theta$$

where n is an integer number of wavelengths, λ is the specific wavelength of the X-ray emitted at the sample, d is the d-spacing between lattice planes, and θ is the incident angle of the X-rays with the sample. Wavelength λ and θ are provided from XRD and used to calculate d spacing. After aligning peaks with probable phases respective peaks and miller indices are determined, these indices are combined with d-spacing to determine the lattice parameter for the material through the following relationship:

$$a = d\sqrt{h^2 + k^2 + l^2}$$

After determining the lattice parameter of the material, the close-pack directional burgers vector can be determined for the specific crystal system of interest. In the case of Grade 91 SS, the dominant phase is BCC ferrite, which burgers vector is determined as follows:

$$b = \frac{a\sqrt{3}}{2}$$

Several equations can be derived from XRD data once the lattice parameter and burgers vectors have been determined which provide approximate values for strain, average crystallite diameter, and dislocation densities [Wen et al., 2013]. These approximations embody the Williamson-Hall plot method of characterization, and the equations that lead to these approximations will be described here to aid in the analysis of XRD. In the Williamson-Hall plot method, a linear trend

line is determined based on the scattered points of each X-ray peak obtained from the material, each point plotted as [4Sinθ, βCosθ] where β is the full width half maximum measurement across each respective peak in radians. The slope of the linear trend line corresponds to the strain ε of the material, while the y-intercept corresponds to an average full width half maximum across all peaks.

Once the Williamson-Hall plot has been constructed, the following approximations can be made. For average crystallite diameter d,

$$d = \frac{K\,\lambda}{\beta}$$

where λ is the x-ray wavelength utilized in the XRD analysis (~0.15418 nm in this case), β is the y-intercept of the Williamson-Hall plot linear trend line, and K is a constant factor ~0.94. For dislocation density:

$$\rho = \frac{2\sqrt{3}\,\varepsilon}{d\,b}10^{18}$$

where ε is the strain (slope of the linear trend line), b is the burgers vector, and d is the estimated crystallite diameter calculated earlier. These approximations can serve as an informative comparison to hardness and TEM data.

3.0 Materials and Methods

3.1 Thermo-mechanical treatments

3.1.1 Grade 91: Normalization and Tempering

The elemental composition of Grade 91 stainless steel can be found in Table 2. The first row indicated the specific matrix of the samples used in this study as provided by the manufacturers, American Alloy Steel. The second row provides the results of an elemental analysis performed by Exova to verify the sample's pedigree.

Table 2: Composition matrix of Grade 91 stainless steel as provided by the vendor (American Alloy Steel), along with EXOVA chemical analysis results for verification.

Elements	C	Mn	P	S	Si	Ni	Cr	Mo	Cu	Nb	V	N
Matrix (wt. %)	0.08	0.53	0.016	0.003	0.28	0.13	8.43	0.9	0.09	0.07	0.225	0.0377
Exova (wt. %)	0.11	0.43	0.01	0.005	0.46	0.17	8.38	0.9	0.17	0.06	0.2	0.03

Because thermo-mechanical treatments can aid in achieving high strength, ductility, and microstructural homogeneity in pure metals and alloys, a series of heat treatments were performed to the samples of Grade 91 in this research [Song et al., 2016]. Grade 91 is designed with stabilizing alloying elements that aid in producing 100% austenite at austenitizing temperatures and 100% martensite upon post-austenitization quenching [Murty et al., 2008]. This process is called normalization, and can lead to the formation of a high dislocation number density in 7-12% Cr steels [Klueh et al., 2007]. For this reason, samples are tempered after normalization, converting most of the martensite into ferrite, simultaneously relaxing many of the dislocations formed during normalization. Also known as tempered martensite, this structure

has a good balance of strength, toughness and ductility. Table 3 provides the specific thermos-mechanical treatments performed on the samples in this work.

Table 3: Thermo-mechanical treatments performed on Grade 91 samples.

Sample	Norm. [°C, min., quench]	Temper [°C, min., quench]	ECAP [℃, route, ϕ, passes]	Anneal [℃, min., quench]
Pre-ECAP	1038, 45, air	788, 45, air	n/a	{600/700/800}, 180, air
ECAP	1050, 60, oil	800, 60, air	300, Bc, 120°, 6	{600/700/800}, 180, air

3.1.2 Experiment: Ex-Situ/In-Situ Thermal Annealing

The thermal annealing holder used is a Hummingbird Scientific high temperature holder. The accompanying control panel is a LabView based software developed by Hummingbird Scientific. This control panel only has temperature-set control, not heating rate control, so in-situ thermal annealing was performed by stair stepping the temperature in 30° C increments during ramp up and cool down.

3.2 Characterization Techniques

3.2.1 Micro-Indentation

A standard mechanical test, micro-hardness acquired through micro-indentation can be loosely correlated to the yield stress of a material using the relationship:

$$\sigma_{yield} \cong \frac{HV}{3}$$

where HV is the hardness value in the Vicker's scale and σ_{yield} is in MPa [Hao et al., 2014; Ivanisenko et al., 2006; Meyers et al., 2006]. This simple technique was utilized to determine hardness evolution of Grade 91 before and after ECAP processing, as well as through post ECAP

annealing through various temperatures. It is expected to see the hardness increase after ECAP processing and decrease after subsequent post ECAP annealing proportional to temperature and annealing time. The micro-indenter used is a LECO Corporation model LM-247AT.

3.2.2 Transmission Electron Microscope

The TEM model used is a Tecnai F30 electron microscope and was operated at an accelerating voltage of 300 kV. The transmission electron microscope (TEM) is a staple characterization method for materials research due to its ability to produce quality imaging of high resolution lattice arrangements, diffraction patterns and rings, and both bright and dark field imaging of microstructures. The image is produced when a high-powered electron beam passes through sample a sufficiently thinned region. TEM is also the base equipment infrastructure on which additional platforms may be appended, such as scanning transmission electron microscopy, energy dispersive spectroscopy, ASTAR, and other packages.

This technique was chosen for this body of research to facilitate comparison between the microstructure evolution of Grade 91 stainless steel before and after ECAP processing, ECAP processing effects under altered parameters, and effects of post ECAP processing thermal annealing. Grain refinement is expected after any ECAP processing, while some grain growth is expected during thermal annealing. Presence of precipitates is also expected in this material. Diffraction patterns and high resolution techniques will be utilized to determine d-spacing of precipitates and aid in phase characterization of precipitates versus bulk matrix composition. Dark field imaging is used to observe grain sizes as a comparison point for ASTAR analysis.

3.2.3 Scanning Transmission Electron Microscope & Energy Dispersive Spectroscopy

Scanning transmission electron microscopy (STEM) and energy dispersive spectroscopy (EDS) work hand in hand to determine the chemical nature of materials of interest. With STEM, a sample can be viewed with z contrast, where heavier elements appear brighter than lighter elements. By this mode, unique precipitates with compositions that deviate from the bulk matrix composition can be clearly observed, their size and distribution density determined. EDS operates by capturing the x-rays emitted by elements excited by the scanning beam of STEM mode and measuring the characteristic energies of the X-rays emitted by the elements of the sample. Energy losses are directly correlated with the elements of the sample to give a chemical spectrum of the selected scan region. Point, line, and operator selected scan regions can be used to observe chemical trends across boundaries and through particles and other features. Although less reliably accurate for light elements such as carbon or silicon, this technique can provide atomic ratio information helpful in determining phase and observe GB segregation, preferential diffusion, and other behaviors. This technique was chosen to assist in determining precipitate composition for phase determination, information required for ASTAR analysis.

3.2.4 ASTAR

ASTAR is a relatively new technique for microstructural-crystallographic characterization that provides information comparable to electron backscatter diffraction (EBSD), namely orientation and phase mapping, texture, and grain size distribution. However, where EBSD requires a highly polished and clean sample surface, a difficult task on its own, ASTAR can be performed on a standard TEM sample with no special regard for surface preparation. With ASTAR, individual crystals do not need to be aligned to a zone axis to obtain diffraction patterns, making this technique ideal for beam sensitive materials such as ferromagnetic Grade 91 [Portillo, 2013].

Originally invented to aid in the characterization of ECAP processed materials with significant grain refinement, ASTAR also has a higher spatial resolution than EBSD (capable of down to 1 nm step sizes compared to >150 nm for EBSD) and relies on diffraction patterns directly instead of Kikuchi lines which can't be obtained from ceramics, severely deformed metals, and other materials.

The technique's software uses cross correlation and optimal template matching to compare acquired diffraction patterns with user provided phase information. A virtual bright field (VBF) image of the scan region is reconstructed by plotting the intensity fluctuations of each diffraction pattern's central spot. The VBF image is more useful than a standard bright field TEM image as the precession of the beam during ASTAR reduces diffraction and curvature contrast [Portillo, 2013].

In summary, less sample prep and scan time, higher resolution, and compatibility with highly deformed, beam sensitive metals with significant grain refinement make ASTAR the preferred technique for orientation crystallography for ECAP processed Grade 91. Furthermore, ASTAR has yet to be performed on Grade 91 stainless steel and will therefore be a highlight of this body of work. It's high resolution will be utilized to further explore the nature of the small precipitates reported in literature [Jones et al., 1991; Shrestha et al., 2015]. The ASTAR system used is a Nanomegas Digistar P1000 and uses the Topspin data collection software.

3.2.5 X-Ray Diffraction

X-ray diffraction (XRD) takes advantage of the angstrom scale wavelength of x-rays (0.01-10nm) and Bragg's Law to measure distances between lattice planes of polycrystalline material. Data produced by XRD works supplementary with TEM-produced diffraction patterns to verify

the phase composition of a given material, and as such will prove instrumental in characterizing the precipitates in Grade 91 stainless steel. It is expected to see peaks corresponding to ferrite (the bulk structure of low carbon steels) and $M_{23}C_6$ phases. The machine used is a Bruker Advanced X-ray Solutions. 2 θ scans were done using 0.6 mm divergence slits, with a scanning speed of 0.01 °/min.

3.2.6 Differential Scanning Calorimetry

Differential scanning calorimetry (DSC) operates by measuring the thermal flux profile of a bulk sample heated and cooled at a steady rate over a set range of temperatures. Peaks and valleys in the profile correspond to phase temperature transitions in the material. This technique will aid in determining the thermal stability of Grade 91 as well as ECAP processed Grade 91. The DSC device used in this study is the Perkin Elmer Simultaneous Thermal Analyzer (STA) 8000. Heating and cooling rates were held identical at 20° C/min. Experiments were run from room temperature to 1100° C and back to room temperature again.

4.0 Development of NSUF ECAP Facility

In addition to performing characterization of ECAP processed Grade 91 produced by Prof. R. Z. Valiev, a fully functional ECAP facility has been constructed in the Center for Advanced Energy Studies to be adopted into the NSUF network. This system is designed to push sample billets of approximate 0.5 in. square cross-sections with gauge length 6 in. through a 120° bend at room temperature, with back pressure applied on the order of the sample's yield strength to reduce sample cracking. As is typical of ECAP systems, this system will be capable of multiple passes and pass routes, depending on the robustness of the material being pressed.

4.1 Design & Operation

The system is composed of a Dake model 8-150 electrically actuated hydraulic press, a 316 SS ram-plunger adaptor, tool steel die and plunger assemblies, and a 316 SS mounting plate. The press is rated to a down force of 150 tons. A back-pressure system designed to reduce sample cracking during extrusion is composed of an Enerpac RD-256 hydraulic cylinder (10.7 ksi rating) powered by an independent Enerpac PUJ-1400B ground pump (see Figure 5). The die is securely mounted to a mounting plate via two steel angle iron braces and four points of contact using ¾ in. Grade 5 bolts.

Figure 10: CAES ECAP System; 1-die, 2-back pressure cylinder, 3-press/plunger, 4-press controls/readouts, 5-back pressure controls/readouts, 6-mounting plate

The die is composed of two halves secured together with sixteen ¾ in. Grade 8 bolts and features a 120° bend. A simplified rendering of the die can be seen in Figure 6. Here it is shown that a sample is inserted through the top of the die. After insertion, the sample makes contact with the back pressure sliding bar. As the sample is extruded, the sliding bar, with a removable backstop

pin (not shown here), is forced to move with the sample while applying an opposing force to the direction of motion. After the sample is fully extruded, the backstop pin is removed to allow the slider bar to fully retract, releasing the sample for retrieval.

Note that a back-pressure system is employed in this ECAP system. This is strategic as it reduces the formation of a "corner gap" or dead zone, where the sample would break contact with the outer corner of the die, leading to inhomogeneity being introduced into the material [Valiev et al., 2006]. According to Prokofiev, E.A. et al., back-pressure can improve general operation by contributing to more crack free passes, a great concern for a room temperature ECAP system [Prokofiev et al., 2014]. Back pressure also contributes to more homogenous and greater levels of grain refinement than if back pressure were not used. Uniform, homogenous microstructure means consistent mechanical properties throughout the sample, an important and desirable trait to strive for when processing materials in bulk. The work of P. Frint et al. showed that back-pressure near the proof stress of the sample yields excellent homogeneity with negligible local

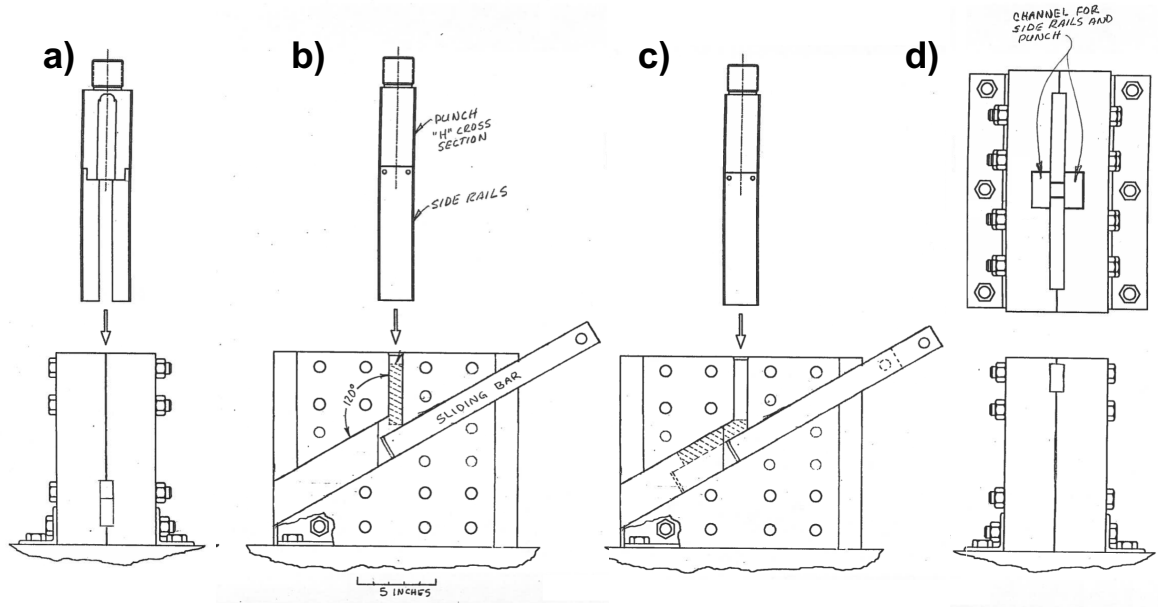

Figure 6: a) front view of plunger/die; b) die internal cutaway view: after sample insertion; c) die internal cutaway view: sample after extrusion; d) top and back view of die showing insertion points for plunger and back pressure sliding bar.

heterogeneity at the bottom of the billet [Frint et al., 2012]. Back-pressure for this system will therefore operate around 415 MPa.

The last controllable parameter of interest is the pressing speed of the ram. R. Z. Valiev et al. have demonstrated that pressing speed seems to have no correlation with the resultant equilibrium grain size formed by ECAP [Valiev et al., 2006]. However, he also suggests that lower speeds (<1in./sec.) may facilitate recovery, allowing the material to reach equilibrium sooner. For this reason, pressing speeds will be kept within this capped range. As with the samples characterized in this work, this ECAP facility will primarily operate with the Bc route for all the reasons mentioned earlier.

4.2 Controls

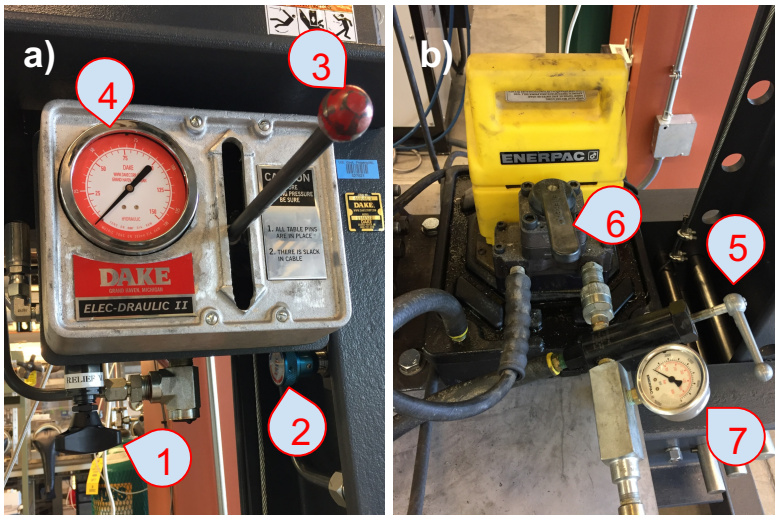

Figure 11: a) Controls and readouts for down pressure system; 1-pressure limiting valve, 2-pressing rate flow control valve, 3-press activation lever, 4-pressure gauge; b) Controls and readouts for back pressure system; 5-pressure limiting valve, 6-forward/reverse direction lever, 7-pressure gauge.

To aid in experimental control of the commercial Dake 150 press, it has been retrofitted with an external system pressure reducing valve and a flow control valve (see Figure 7). These control the plunger's down pressure limit and the pressing rate, respectively. Down pressure can be

monitored real time via the presses' built in pressure gauge. Pressing speed must be measured and calibrated prior to extrusion. Because the back-pressure system is powered by an independent pump, it has separate controls and readouts. A pressure reducing valve determines how much back pressure is to be applied as monitored by the back-pressure system gauge. A three-way valve determines the direction of motion of the double-acting slider bar, i.e. used to pull the sample during extrusion and push the sample out for retrieval after extrusion.

4.3 Safety

Several safety features have been incorporated into this facility. First and foremost, after sample insertion and prior to extrusion, a guarding tube is installed around the entire plunger assembly and secured to the top of the die to enclose all active pinch points (see Figure 8). This guarding also contains a polycarbonate viewing window so the operator can see when the plunger has

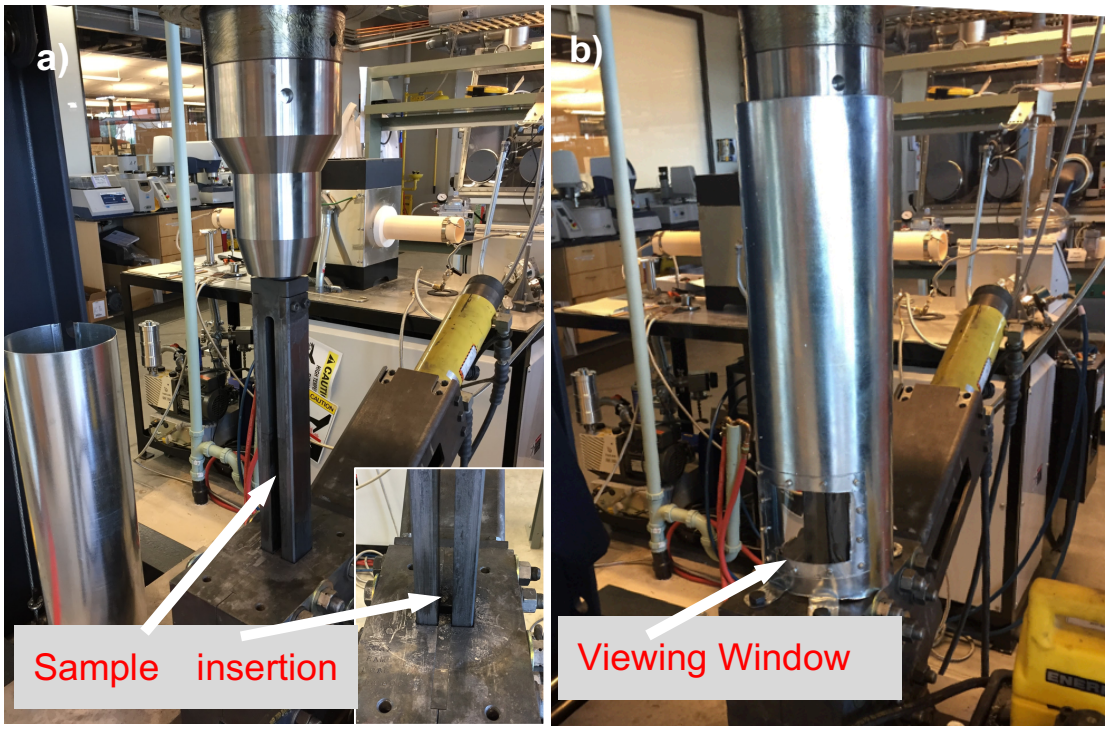

Figure 8: a) Exposed ram-plunger adapter/plunger assembly; b) showing shielding, complete with polycarbonate viewing window, installed after sample insertion prior to pressing.

reached its full down position. The Dake 8-150 press and Enerpac PUJ-1400B ground pump each have their own built in safety features that work in conjunction. The ground pump's toggle control tether and the press activation lever default to a neutral position; Once released, extrusion terminates.

5.0 Analysis of Results

5.1 DSC results

DSC was performed on pre/post ECAP processed Grade 91 to determine phase transition temperatures in the material. Upon heating, it was found that the Curie temperature for pre-ECAP Grade 91 is 756 C, with an austenitation temperature of 874 C (see Figure 9). Temperature transitions for ECAP Grade 91 were 752 and 848 C, respectively. The cooler transition temperatures in the ECAP sample could be attributed to contributions from stored

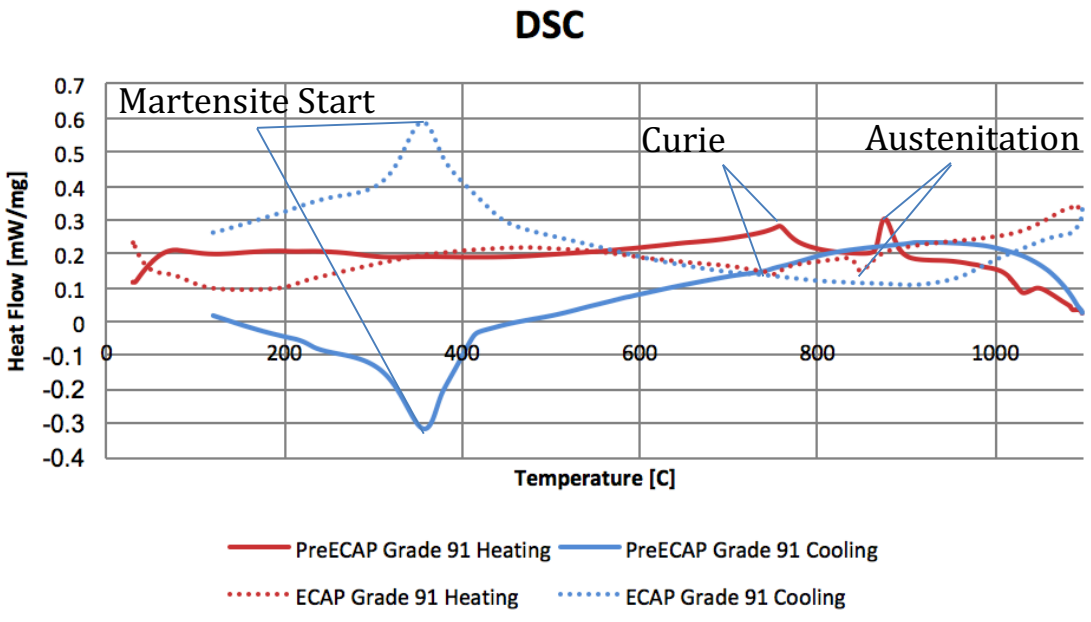

Figure 9: DSC results indicate that both Curie and austenitation temperatures are slightly lower for ECAP processed grade 91. This is possibly due to contributions from interfacial strain energies induced by ECAP shearing.

strain energy imposed by the severe plastic deformation imposed by ECAP processing. Upon cooling, a martensitic transformation occurs at 355 and 357 C for pre- and post-ECAP processed Grade 91, respectively. The close agreement of the two martensitic transformation temperatures suggests that once fully austenetized, the bulk of the strains imposed by ECAP has been relaxed.

5.2.1 TEM results: Pre/Post-ECAP Grade 91

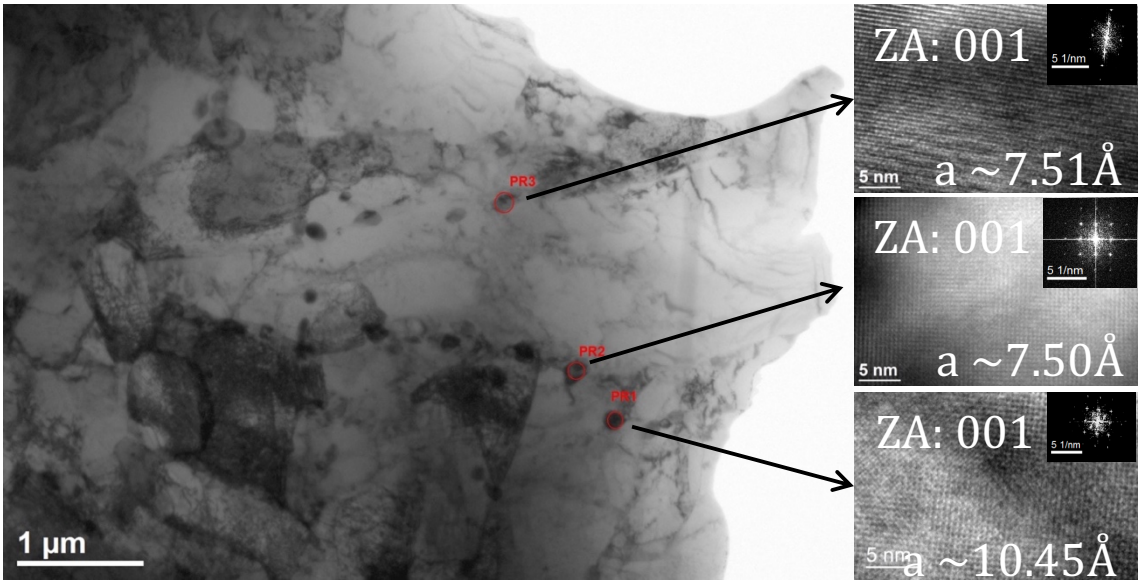

Figure 10: TEM micrograph of pre-ECAP Grade 91 showing two distinct precipitate types. Lattice parameter ~10.45Å corresponds to $Cr_{23}C_6$ phase (lattice parameters calculated from FFT measurements of high resolution imaging).

3 mm diameter TEM samples were prepared using mechanical grinding and polishing to a thickness of ~30 µm. Subsequent milling by a precision ion polishing system (PIPS) was performed with an ionizing voltage of 5 keV at 8° offset for ~45-60 min., followed by a thinning pass with 3 keV at 2° offset for 5 min., to create a hole with an inside edge sufficiently thin for TEM viewing. TEM was performed to obtain low magnification images, high magnification images, and selected area diffraction patterns to aid in the characterization of pre/post-ECAP Grade 91. In pre-ECAP Grade 91, precipitates were observed along what appear to be former austenitic GBs (See Figure 10). High resolution imaging of these precipitates, and subsequent

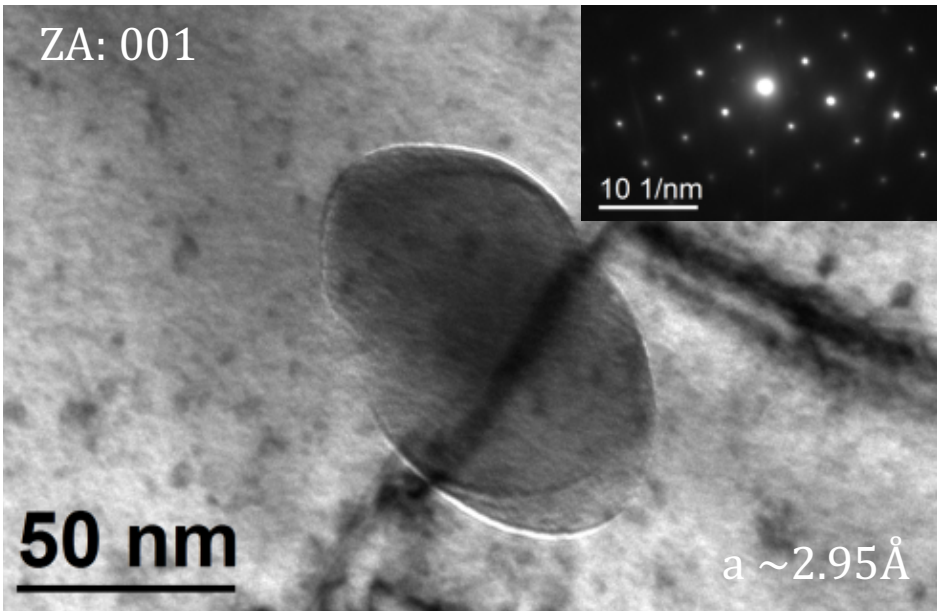

Figure 11: Converged beam diffraction of a third precipitate type.

fast Fourier transform (FFT) processing to obtain diffraction spots, lead to measurements determining lattice parameters consistent with the $M_{23}C_6$ carbide structure (a~10.45Å) mentioned in the literature [Klueh et al., 2007; Maier et al., 2013]. Other precipitates were found, however, with lattice parameters inconsistent with structures reported by others, evaluated at ~2.95Å and 7.5Å (See Figures 10,11). These were compared against the Pearson's crystal database through various other reported precipitate structures of $M_{23}C_6$ (Cr, Fe, or Mo carbide) and MX (V or Nb, and C or N). [Klueh et al., 2007; Song et al., 2013]. No verifiable matches were found. These structures are still unidentified. It is, however, possible that the precipitate in Figure 11 is merely surface contamination overlying the bulk matrix of BCC iron, as ~2.95Å closely approximates the lattice parameter of iron, being ~2.87Å [Ivanisenko et al., 2006].

In the ECAP-processed Grade 91 sample, significant grain refinement was observed (See Figure 12). Average grain size was difficult to determine, owing to the many dislocation networks and cells, sub grains, and other distortions. But, the grain refinement effectively produced relatively equiaxed UFG structures and, based on the completeness of the diffraction rings, a high-volume fraction of HAGBs. These results have been reported in other ECAP processed materials as well [Sklenicka et al., 2013].

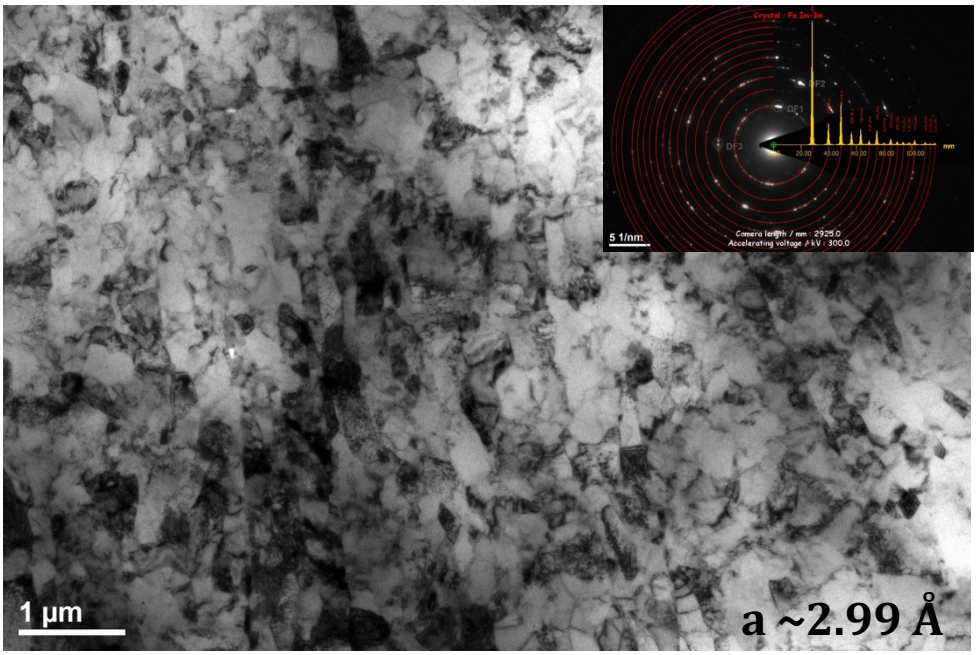

Figure 12: Transverse plane of ECAP processed Grade 91. LADP reveals predominantly ferrite structure. Diffraction rings denote the presence of high volume fraction of HAGBs.

The characteristic precipitates of the pre-ECAP microstructure were no longer visible. This annihilation of precipitates could possibly be caused by their being refined too small to be seen easily or their being re-dissolved back into solid solution when subjected to ECAP-induced SPD, though the specific mechanism cannot be determined from these results. Former austenite GBs are also no longer visible in ECAP-processed Grade 91. This result is consistent with the work of M. Song et al. who found that when processing Grade 91 with ECAP at elevated temperatures,

the elimination of prior austenite GBs contributed to the refinement of precipitates [Song et al., 2013].

5.2.2 TEM results: In-situ thermal annealed ECAP Grade 91

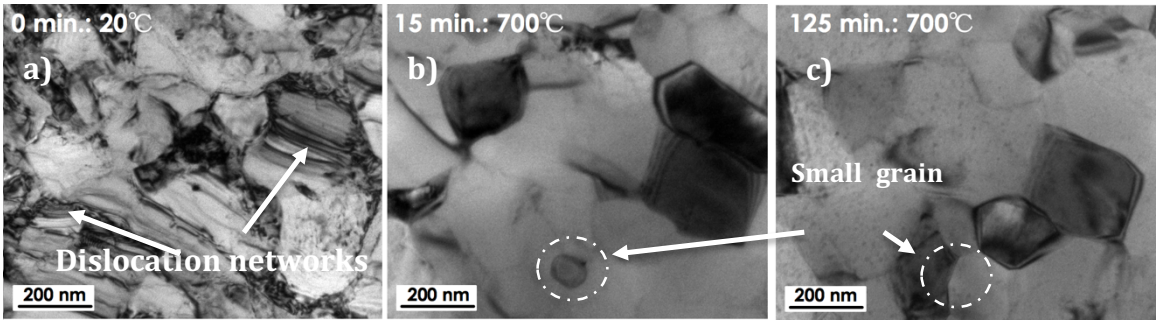

Figure 13: TEM micrographs of ECAP processed Grade 91 through various stages of in-situ thermal annealing. a) As processed ECAP Grade 91 at room temperature; b) After temperature ramp up to 700° C, ~15 minutes; c) After two hours at 700° C.

In-situ thermal annealing was performed on TEM discs prepared as described earlier. Using the Hummingbird Scientific high temperature holder with the accompanying Hummingbird Scientific control panel software, the sample was heated to 700° C over the course of 15 minutes. Heating rate could not be controlled directly, so the temperature of the sample was incrementally increased by 23° every 30 seconds to approximate a linear thermal profile. Care was taken to make micro-adjustments to the TEM stage to keep the sample feature of interest centered, as thermal effects caused the sample to drift during heating. After the sample reached 700° C, this temperature was held for two hours. TEM micrographs were taken every five minutes of operation. Figure 13 provides a summarized view of the microstructural evolution of ECAP-processed Grade 91 as it was annealed.

Prior to annealing, several dislocation networks could be observed throughout the bulk matrix. These were largely annihilated in the first 15 minutes of annealing time as the sample ramped up

to annealing temperature. During the next 2 hours, very little evolution occurred; Only a single small grain, ~100 nm diameter, was consumed by neighboring grains. This trend of very little grain growth up to 700° C and significant reduction in dislocations was also observed by T. Hao et al. [Hao et al., 2014].

By comparison, a digital micrograph was taken of a sample prepared from bulk ECAP Grade 91 subjected to ex-situ thermal annealing under identical conditions (see Figure 14). In this case, significant grain growth was observed (>1 μm grains in some areas) and large precipitates were nucleated back into to sample, both along grain boundaries and within grains themselves along what appear to be fine sub-grains.

These differing results could be explained by the influence of strong surface effects during in-situ annealing and the fact that grain rotations, GB sliding, and other modes of motion during annealing and recovery are limited to nearly a single thin plane in a TEM sample, behaving as a thin film as opposed to the 3-dimensional growth potential in a bulk sample. M. Song et al.

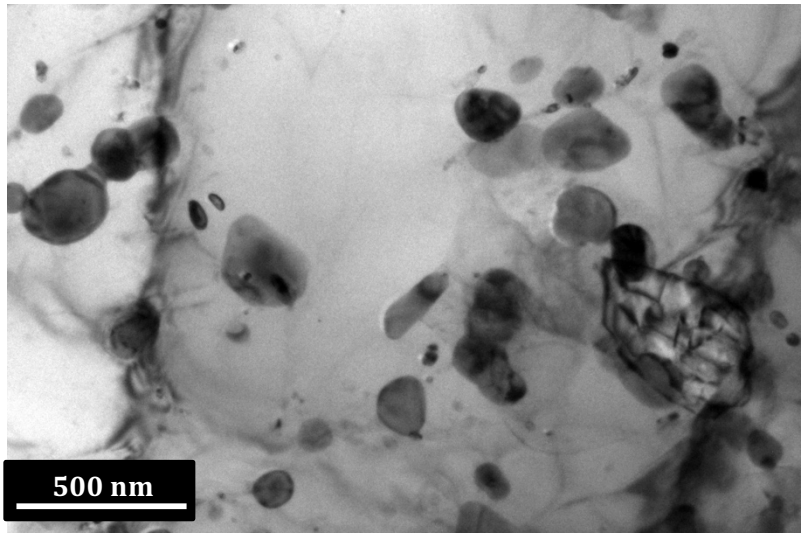

Figure 14: TEM micrograph of post-ECAP Grade 91 ex-situ thermal annealed to 700° C for two hours. Several precipitates intragranular precipitates nucleate and form during annealing.

reported a similar phenomenon in ECAP Grade 91 annealed at 500° C for 10 hours, attributing the precipitation in these locations to the preferential carbon diffusion to prior austenite GBs via pipe and GB-assisted diffusion routes [Song et al., 2013].

5.3 EDS results

EDS was performed only on pre-ECAP Grade 91 as precipitates were no longer visible after ECAP processing. Two main types of precipitates were found using these scans, namely V enriched and Cr enriched particles roughly ~100 nm in diameter. (see Figures 15, 16). Between the two types, Cr enriched precipitates displayed higher atomic percent concentrations than V enriched precipitates. Compositional ratios of these metals with respect to lighter elements (C, Si, N, O) were deemed unreliable as the accuracy of lighter element counts is low with EDS scanning. However, the presence of these enriched Cr and V enriched particles does seem to verify the work done by R.L. Klueh et al., who found Cr enriched precipitates, with an $M_{23}C_6$ structure, and V enriched precipitates with an MX structure (X being C or N) were present in tempered Grade 91 [Klueh et al., 2007].

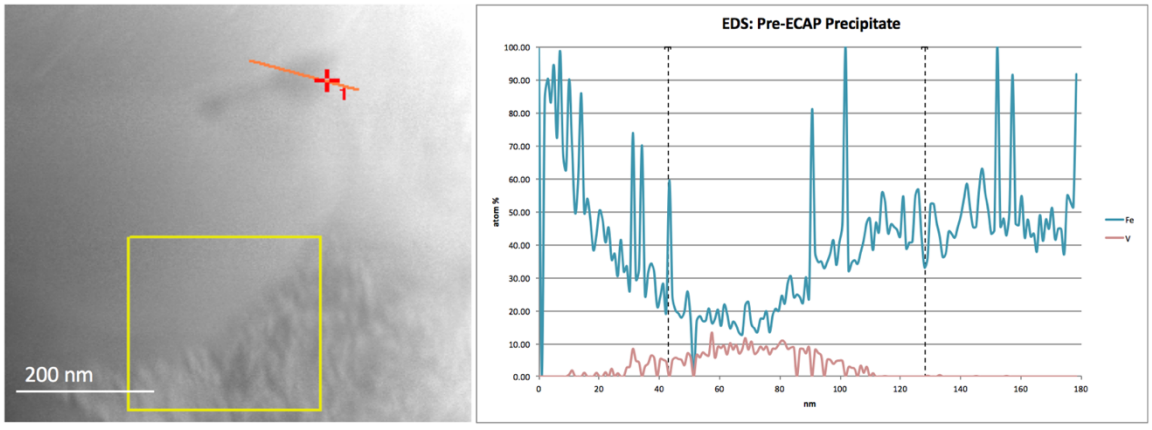

Figure 12: Energy dispersive spectroscopy line scan of pre-ECAP Grade 91 precipitate showing significant V enrichment.

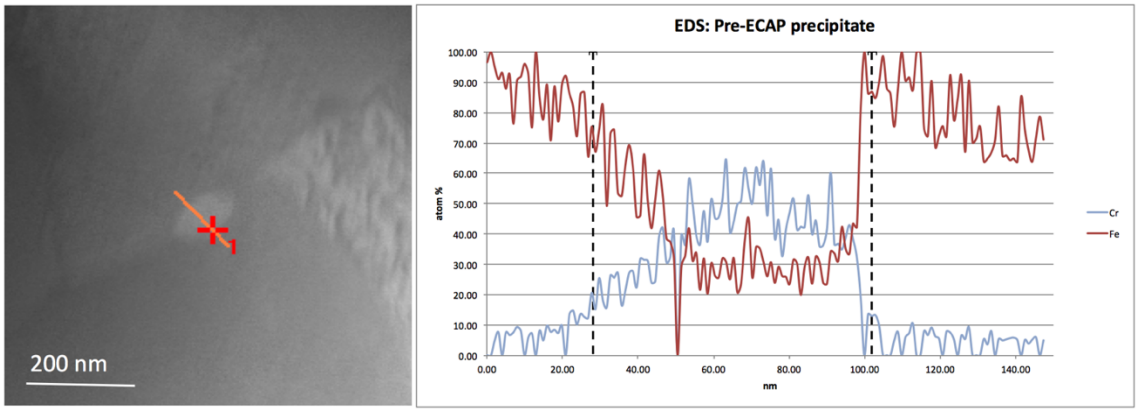

Figure 16: Energy dispersive spectroscopy scans reveal significantly Cr enriched precipitates along GBs.

5.4 XRD results

Samples were prepared for XRD analysis using mechanical polishing, ending in a final polish using 0.05 μm colloidal alumina. XRD results for both pre- and post-ECAP processed Grade 91 resulted in only ferrite peaks, the 110, 200, and 211 planes. No precipitate phase peaks were present. This is possibly due to the precipitates occupying such a small volume fraction that

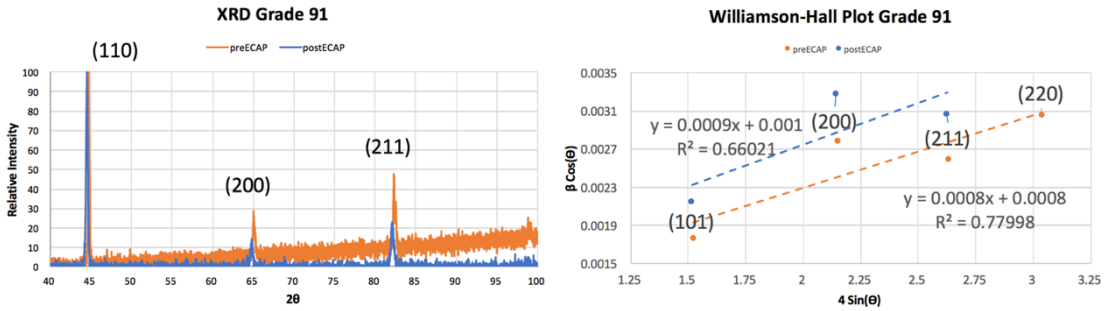

Figure 17: XRD data of Pre/Post ECAP Grade 91; a) Energy spectrum shows only ferrite planes.; b) Williamson-Hall plot derived from XRD data.

reflected X-ray peaks were too small to be determined and were lost in the noise of the device. There is also a noticeable difference in peak heights between pre/post-ECAP XRD spectra. This could be an indication of grain orientation shifting caused by texturing effects [Muralidhar et al., 2013].

Using the Williamson-Hall method for XRD analysis, it was determined that higher strain (+12.5%) and dislocation density (+40.26%) accompany ECAP processing, as well as smaller average crystallite diameters (-20%) (see Table 4). These trends are to be expected from severe plastic deformation. It should be noted that the crystallite diameters determined using the Williamson-Hall method are smaller than those measured in TEM. This is because XRD measures not only incoherent grains, but also coherent diffraction domains such as sub-grains and dislocation cells [Wen et al., 2013].

Table 4: Microstructural characteristics derived from Williamson-Hall plot based approximations.

Sample	Strain %	Size (nm)	Dislocation density (/mm^2)
Pre-ECAP Grade 91	0.08%	181.162	6.16E+13
ECAP Grade 91	0.09%	144.929	8.64E+13

5.5 Hardness results

Pre-ECAP and post-ECAP Grade 91 SS samples were mechanically polished for hardness testing. Vickers hardness was measured using Vickers micro-indenter, operated with an applied force of 300 gf for a dwell time of 13 seconds. Hardness values were averaged over four to five indentations per sample at thirty minutes, one hour, and two hours for each annealing temperature for both pre/post ECAP-processed samples (see Figure 18).

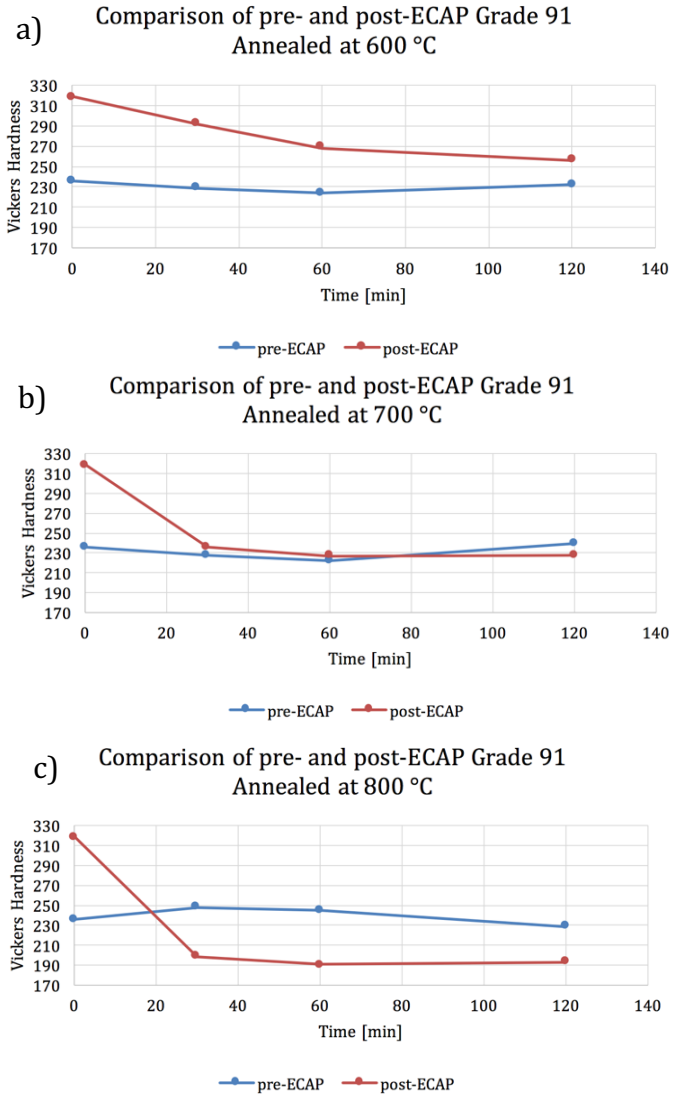

Figure 18: Micro-hardness testing results of pre/post ECAP processed Grade 91 after annealing at a) 600° C, b) 700 c) 800° C.

Prior to annealing, it was observed that ECAP processing resulted in a 35% increase in micro-hardness (corresponding to an estimated yield strength ~1.07 GPa compared to ~0.78 GPa for pre-ECAP Grade 91). Smaller grain size, higher strains, and precipitate hardening were all considered contributing factors to this significant increase. Worthy of noting here is that the Hall-Petch relationship, which states that hardness is inversely proportional to square root of the grain size, remains valid in this instance [Hu et al., 2017]. This is because the microstructure of

the ECAP-processed Grade 91 of this study remains in the UFG regime, whereas the Hall-Petch relationship breaks down only once a microstructure enters the nano-crystalline regime (<25 nm) [Prados et al., 2008].

Once annealing commenced, hardness of pre-ECAP Grade 91 remained relatively stable, regardless of annealing temperature or time annealed. ECAP-processed Grade 91, on the other hand, saw rapid decreases in hardness after the first half hour at elevated temperatures (700°, 800° C) and a noticeable decline at lower temperatures (600° C). Hardness of ECAP-processed Grade 91 quickly reached steady state after the first hour of annealing time. This trend of a rapid decline in hardness toward a steady state, coupled with the observations from both in- and ex-situ thermal annealing experiments showing rapid initial dislocation annihilation and subsequent grain growth, would seem to indicate that dislocations and grain refinement are the dominant hardening factors in ECAP-processed Grade 91. This result verifies results obtained by others [Hao et al., 2014; Song et al., 2013]. It would appear as though hardness approaches steady state as grain growth saturates.

At 700° C, ECAP-processed Grade 91 reached a steady state hardness value comparable to that of pre-ECAP processed Grade 91. At 800° C, however, stored interfacial energy in the form of HAGBs lead to excessive recovery, resulting in a 15.7% reduced hardness value in ECAP-processed Grade 91 compared to its pre-ECAP processed counterpart annealed under the same conditions.

5.6 ASTAR results

ASTAR scans were performed on pre/post-ECAP processed Grade 91 along the extruded plane, and along the transverse plane of post-ECAP processed Grade 91. This last scan was conducted to observe any texturing that may have been generated during the extrusion process. A step size of 10 nm was used for all scans.

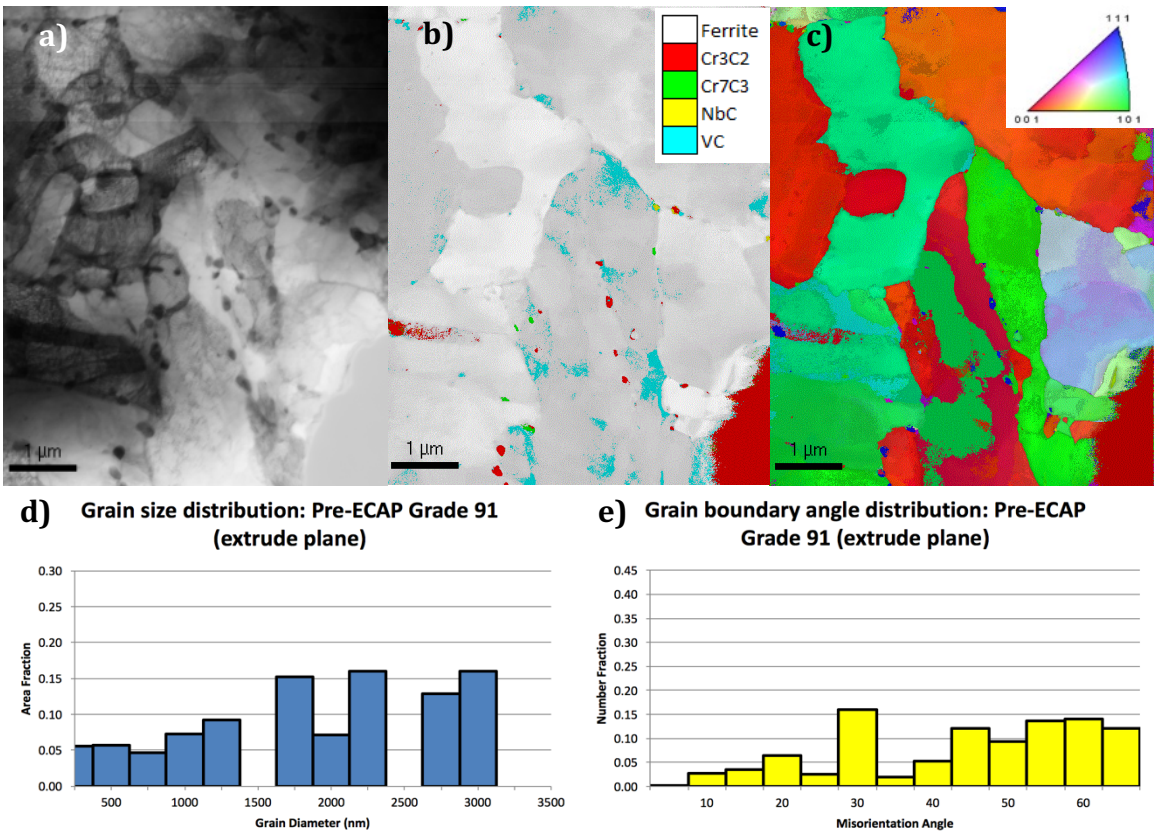

Figure 19: ASTAR scanning on the extrusion plane of pre-ECAP Grade 91

In pre-ECAP Grade 91, Cr_3C_2 was the predominant precipitate structure found, located along former austenite GBs (see Figure 19a, b). Very few Cr_7C_3 and NbC was found. Although EDS scans showed V enriched fine particles, the ASTAR results were less defined, assigning diffuse regions to the VC structure. These results are under question and suspected to be a software matching error more than a definitive microstructural feature. Analysis of these results using OIM software

showed that the grain size distribution of the bulk matrix is ~500-3000 nm, with precipitates ~50-200 nm (Figure 19c). There was also a fairly spread out distribution of GB mis-orientation angles.

In the ECAP Grade 91 virtual bright field image, there is no sign of the continued presence of former austenite GBs (see Figure 20a). The phase map of this sample reflects the same as precipitates are more randomly dispersed compared to the more ordered lines of precipitates seen in pre-ECAP Grade 91 (see Image 19b). Also in the phase map, there appears to be a smaller area fraction of precipitates than in its pre-ECAP counterpart. No Cr_7C_3 was detected and the VC carbide data was more reasonable. Grain size and GB mis-orientation angle distribution analysis reveal significant grain refinement (a high area fraction being <500 nm) and a high density of HAGB (see Figure 20d and e respectively). This confirms the work of M. Song et al. in their claim that the Bc route is effective for populating a sample with HAGBs [Song et al., 2013].

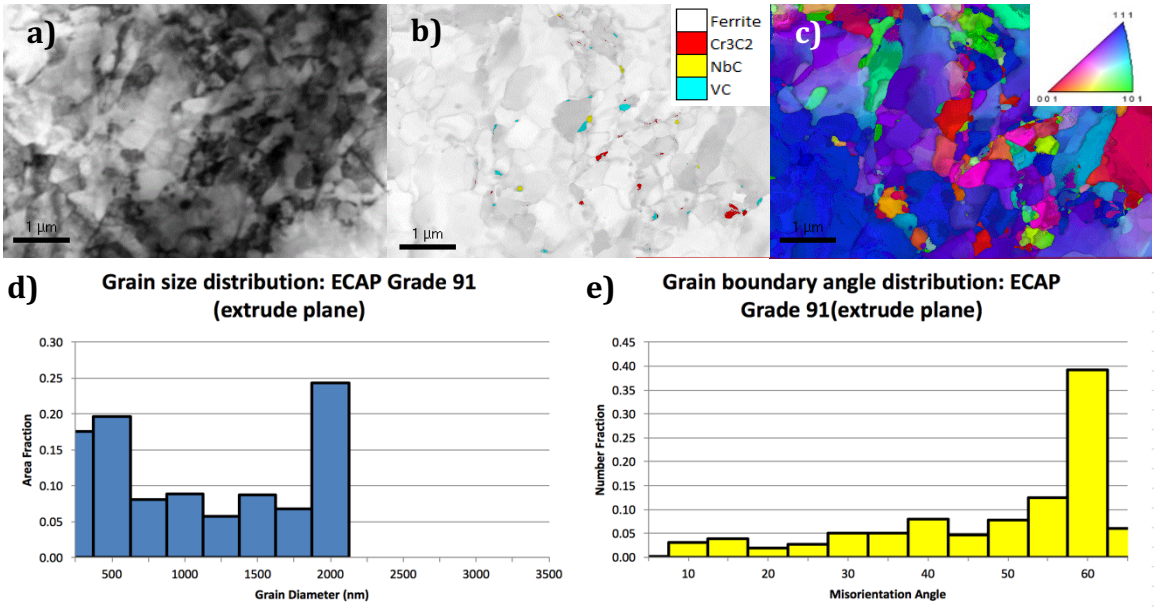

Figure 20: ASTAR scanning on the extrusion plane of post-ECAP Grade 91

The last scan performed, along the transverse plane of ECAP-processed Grade 91, did in fact reveal some texturing along the extrusion axis as seen from the elongated grain structures in the orientation map (see Figure 21). This behavior of texturing along the extrusion axis has also been observed in other materials processed with different ECAP routes [Prados et al., 2008]. Worth mentioning here is that the $M_{23}C_6$ carbide structure most widely reported in literature was not found in any of the ASTAR scans performed. This may, however, be attributed to a software matching issue rather than a true reflection of present precipitate structures.

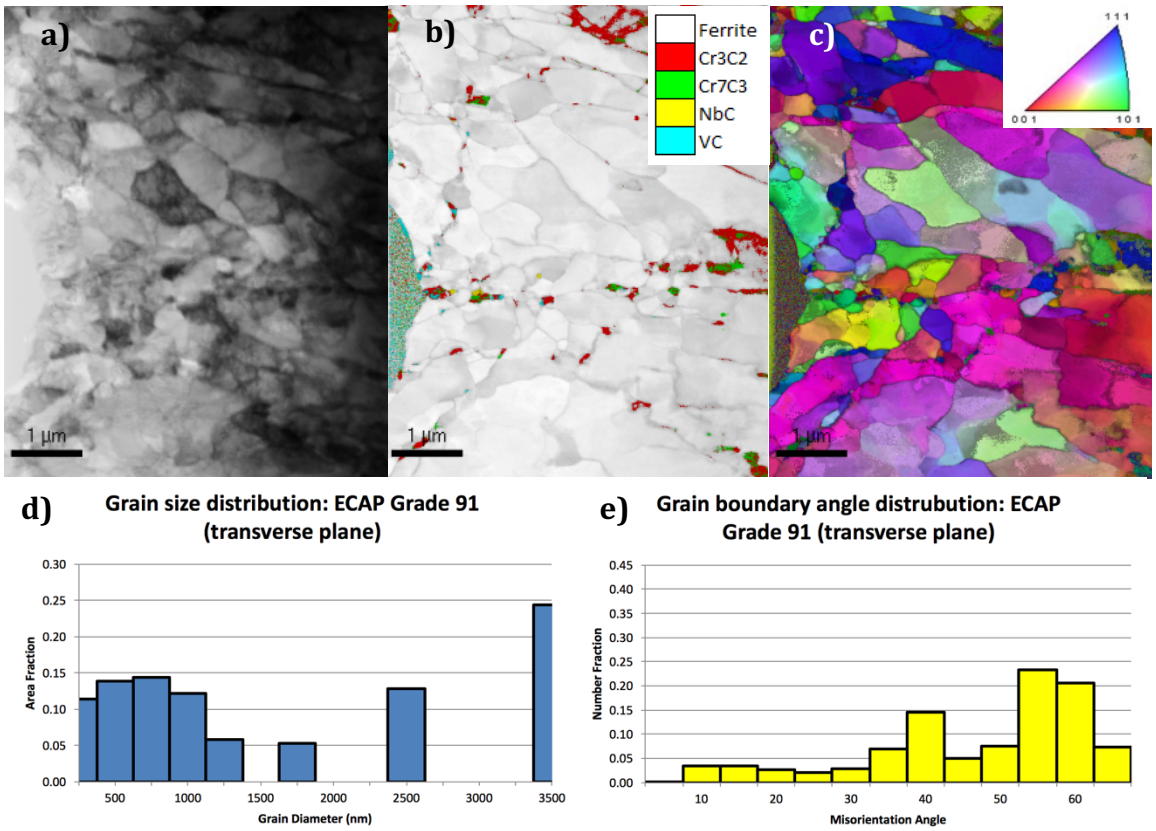

Figure 21: ASTAR scanning on the transverse plane of pre-ECAP Grade 91

6.0 Conclusions

Most of the characterization results of this work were in direct agreement with the work performed by others previously. This agreement, if nothing else, shows the consistency in which

Grade 91 may be processed with ECAP to obtain UFG material. However, the apparent partial elimination of carbides post-ECAP processing suggests that ECAP Grade 91 may not have the carbide strengthened characteristics hoped for to pin the grains for additional thermal stability. ASTAR was proven as an effective technique for generating phase and orientation maps of severely deformed material with fine precipitates. ASTAR also verified the presence of refined grains and a high-volume fraction of HAGBs after ECAP processing, as well as texturing along the transverse plane. However, software matching errors are suspect as expected prominent carbide structures known in Grade 91 were not observed in these ASTAR scans. Although in-situ thermal annealing showed a thermally stable UFG structure in ECAP-processed Grade 91 up to 700° C, the ex-situ thermal annealing results were more reflective of the thermal effects on bulk geometries typical of structural materials. Hardness results of ex-situ thermally annealed samples revealed that ECAP-processed Grade 91 was only stable at 600° C, making this material most suitable for sodium cooled fast reactors. Most surprising, however, was the discovery of precipitates with unique lattice parameters that didn't conform to the $M_{23}C_6$ or MX precipitate structures expected in Grade 91.

6.1 Future Work

Many of the challenges involved in the characterization in this study revolved around Grade 91's ferromagnetic properties. By using standard sized TEM discs (3 mm diameter prepared with PIPS), there was significant sample mass and thickness to make high resolution imaging of precipitates aligned with a zone axis very difficult, as any rotation of the sample would severely deflect the TEM's electron beam. The thickness of the samples also made finding precipitates and other structures in STEM mode nearly impossible. Perhaps using TEM lamellas made by

focused ion beam techniques would yield better results as they are thinner and made of considerably less material.

This study was intended to be a simple baseline characterization, not a fully comprehensive examination. To further round out this work, however, in-situ annealing at both 600° and 800° C could be conducted and TEM imaging of the already performed ex-situ annealed samples at these temperatures could be acquired. ASTAR scans of annealed ECAP samples could reveal more about the nature of the intragranular precipitation of carbides observed in TEM. Because the XRD analysis failed to pick up on precipitate phases, and because EDS-produced atomic composition ratios are unreliable for lighter elements such as carbon, synchrotron analysis is being considered to obtain a more definitive characterization of all present phases. This would greatly enhance analysis of ASTAR scans to determine precipitate distributions.

Regarding the Idaho National Labs based ECAP facility, copper stock will be extruded in August 2018 as an initial test of its efficacy for refining grain structures. After that, as received Grade 91 bar stock will be extruded to aid in further characterization efforts. The system has also been designed to be easily retrofitted for elevated temperature extrusions, a feature that may be added in the future.

References

[1] Bachhav, M., Robert Odette, G., & Marquis, E. A. (2014). a' precipitation in neutron-irradiated Fe-Cr alloys. *Scripta Materialia*, *74*, 48–51. https://doi.org/10.1016/j.scriptamat.2013.10.001

[2] Bachhav, M., Yao, L., Robert Odette, G., & Marquis, E. A. (2014). Microstructural changes in a neutron-irradiated Fe-6 at.%Cr alloy. *Journal of Nuclear Materials*, *453*(1–3), 334–339. https://doi.org/10.1016/j.jnucmat.2014.06.050

[3] Chen, Y. (2013). Irradiation effects of HT-9 martensitic steel. *Nuclear Engineering and Technology*, *45*(3), 311–322. https://doi.org/10.5516/NET.07.2013.706

[4] Djavanroodi, F., Sedighi, M., Hashemi, P., & Ebrahimi, M. (2014). Equal channel angular pressing of copper wire. *Proceedings of the Institution of Mechanical Engineers, Part B: Journal of Engineering Manufacture*, *228*(10), 1273–1279. https://doi.org/10.1177/0954405413517495

[5] Fan, Z. Q., Hao, T., Zhao, S. X., Luo, G. N., Liu, C. S., & Fang, Q. F. (2013). The microstructure and mechanical properties of T91 steel processed by ECAP at room temperature. Journal of Nuclear Materials, 434(1–3), 417–421. https://doi.org/10.1016/j.jnucmat.2012.12.009

[6] Frint, P., Hockauf, M., Halle, T., Wagner, M. F. X., & Lampke, T. (2012). The role of backpressure during large scale Equal-Channel Angular Pressing. Materialwissenschaft Und Werkstofftechnik, 43(7), 668–672. https://doi.org/10.1002/mawe.201200015

[7] Hao, T., Fan, Z. Q., Zhao, S. X., Luo, G. N., Liu, C. S., & Fang, Q. F. (2014). Strengthening mechanism and thermal stability of severely deformed ferritic/martensitic steel. Materials Science and Engineering A, 596, 244–249. https://doi.org/10.1016/j.msea.2013.12.062

[8] Hu, J., Shi, Y. N., Sauvage, X., Sha, G., & Lu, K. (2017). Grain boundary stability governs hardening and softening in extremely fine nanograined metals. Science (New York, N.Y.), 355(March), 1292–1296. https://doi.org/10.1126/science.aal5166

[9] Huang, C. X., Gao, Y. L., Yang, G., Wu, S. D., Li, G. Y., & Li, S. X. (2006). Bulk nanocrystalline stainless steel fabricated by equal channel angular pressing. *Journal of Materials Research*, *21*(07), 1687–1692. https://doi.org/10.1557/JMR.2006.0214

[10] Huang, C. X., Yang, G., Deng, B., Wu, S. D., Li, S. X., & Zhang, Z. F. (2007). Formation mechanism of nanostructures in austenitic stainless steel during equal channel angular pressing. *Philosophical Magazine*, *87*(31), 4949–4971. https://doi.org/10.1080/14786430701594046

[11] Ivanisenko, Y., MacLaren, I., Sauvage, X., Valiev, R. Z., & Fecht, H. J. (2006). Shear-induced alpha -> gamma transformation in nanoscale Fe-C composite. *Acta Materialia*, *54*(6), 1659–1669. https://doi.org/10.1016/j.actamat.2005.11.034

[12] Jones, W. B., Hills, C. R., & Polonis, D. H. (1991). Microstructural evolution of modified 9Cr-1Mo steel. *Metallurgical Transactions A*, *22*(5), 1049–1058. https://doi.org/10.1007/BF02661098

[13] Kim, H. S. (2001). Finite element analysis of equal channel angular pressing using a round corner die. Materials Science and Engineering A, 315(1–2), 122–128. https://doi.org/10.1016/S0921-5093(01)01188-1

[14] Klueh, R. L., & Nelson, A. T. (2007). Ferritic/martensitic steels for next-generation reactors. *Journal of Nuclear Materials*, *371*(1–3), 37–52. https://doi.org/10.1016/j.jnucmat.2007.05.005

[15] Maier, G. G., Astafurova, E. G., Maier, H. J., Naydenkin, E. V., Raab, G. I., Odessky, P. D., & Dobatkin, S. V. (2013). Annealing behavior of ultrafine grained structure in low-carbon steel produced by equal channel angular pressing. Materials Science and Engineering A, 581, 104–107. https://doi.org/10.1016/j.msea.2013.05.075

[16] Meyers, M. A., Mishra, A., & Benson, D. J. (2006). Mechanical properties of nanocrystalline materials. Progress in Materials Science. https://doi.org/10.1016/j.pmatsci.2005.08.003

[17] Muralidhar, A., Narendranath, S., & Shivananda Nayaka, H. (2013). Effect of equal channel angular pressing on AZ31 wrought magnesium alloys. Journal of Magnesium and Alloys, 1(4), 336–340. https://doi.org/10.1016/j.jma.2013.11.007

[18] Murty, K. L., & Charit, I. (2008). Structural materials for Gen-IV nuclear reactors: Challenges and opportunities. *Journal of Nuclear Materials*, *383*(1–2), 189–195. https://doi.org/10.1016/j.jnucmat.2008.08.044

[19] Murty, K. L., & Charit, I. (2013). An introduction to nuclear materials fundamentals and applications.

[20] Nashith, A., Sanjid, P., Shamsudheen, M., Rasheeque, R., Ramis, M. K., & Shebeer, A. R. (2014). Effect of Equal Channel Angular Pressing (ECAP) on Hardness and Microstructure of Pure Aluminum, *4*(3), 119–122. https://doi.org/10.5923/j.ijme.20140403.08

[21] Portillo, J. (2012). Precession Electron Diffraction in the Transmission Electron Microscope : electron crystallography and orientational mapping. *Capítol Del Llibre: Handbook of Instrumental Techniques for Materials, Chemical and Biosciences Research, Centres Científics i Tecnològics. Universitat de Barcelona, Barcelona, 2012. Part I. Materials Technologies (MT), MT.3, 10 P.*, 1–3.

[22] Prados, É. F., Sordi, V. L., & Ferrante, M. (2008). Microstructural development and tensile strength of an ECAP: deformed Al-4 wt. (%) Cu alloy. Materials Research, 11(2), 199–205. https://doi.org/10.1590/S1516-14392008000200015

[23] Prokofiev, E. A., Jorge, A. M., Botta, W. J., & Valiev, R. Z. (2014). Development of Ultrafine-Grained Metals by Equal-Channel Angular Pressing. In *Comprehensive*

Materials Processing(pp. 187–209). Elsevier. https://doi.org/10.1016/B978-0-08-096532-1.00314-9

[24] Rifai, M., Miyamoto, H., & Fujiwara, H. (2014). Effect of deformation route on the development of low CN Fe-20%Cr alloy by Equal Channel Angular Pressing. *IOP Conference Series: Materials Science and Engineering*, *63*, 012122. https://doi.org/10.1088/1757-899X/63/1/012122

[25] Rifai, M., Miyamoto, H., & Fujiwara, H. (2014). The Effect of ECAP Deformation Route on Microstructure, Mechanical and Electrochemical Properties of Low CN Fe-20%Cr Alloy. *Materials Sciences and Applications*, *5*, 568–578. https://doi.org/10.4236/msa.2014.58059

[26] Shin, H. C., Ha, T. K., Park, W. J., & Chang, Y. W. (2003). Deformation-Induced Martensitic Transformation under Various Deformation Modes. *Key Engineering Materials*, *233–236*, 667–672. https://doi.org/10.4028/www.scientific.net/KEM.233-236.667

[27] Shrestha, T., Alsagabi, S., Charit, I., Potirniche, G., & Glazoff, M. (2015). Effect of Heat Treatment on Microstructure and Hardness of Grade 91 Steel. *Metals*, *5*(1), 131–149. https://doi.org/10.3390/met5010131

[28] Sklenicka, V., Dvorak, J., Svoboda, M., Kral, P., & Kvapilova, M. (2013). Equal-channel angular pressing and creep in ultrafine- grained aluminium and its alloys. Aluminum Alloys, 3–46. https://doi.org/1372CEA0E1BB853588B8A84E3AE0450E

[29] Song, M., Zhu, R., Foley, D. C., Sun, C., Chen, Y., Hartwig, K. T., & Zhang, X. (2013). Enhancement of strength and ductility in ultrafine-grained T91 steel through thermomechanical treatments. Journal of Materials Science, 48(21), 7360–7373. https://doi.org/10.1007/s10853-013-7522-3

[30] Song, M., Wu, Y. D., Chen, D., Wang, X. M., Sun, C., Yu, K. Y., … Zhang, X. (2014). Response of equal channel angular extrusion processed ultrafine-grained T91 steel subjected to high temperature heavy ion irradiation. Acta Materialia, 74, 285–295. https://doi.org/10.1016/j.actamat.2014.04.034

[31] Song, M., Sun, C., Fan, Z., Chen, Y., Zhu, R., Yu, K. Y., … Zhang, X. (2016). A roadmap for tailoring the strength and ductility of ferritic/martensitic T91 steel via thermo-mechanical treatment. Acta Materialia, 112, 361–377. https://doi.org/10.1016/j.actamat.2016.04.031

[32] Sun, C., Zheng, S., Wei, C. C., Wu, Y., Shao, L., Yang, Y., … Zhang, X. (2015). Superior radiation-resistant nanoengineered austenitic 304L stainless steel for applications in extreme radiation environments. *Scientific Reports*. https://doi.org/10.1038/srep07801

[33] Valiev, R. Z., Islamgaliev, R. K., & Alexandrov, I. V. (2000). Bulk nanostructured materials from severe plastic deformation. Progress in Materials Science(Vol. 45). https://doi.org/10.1016/S0079-6425(99)00007-9

[34] Valiev, R. Z., & Langdon, T. G. (2006). Principles of equal-channel angular pressing as a processing tool for grain refinement. Progress in Materials Science, 51, 881–981. https://doi.org/10.1016/j.pmatsci.2006.02.003

[35] Wen, H., Topping, T. D., Isheim, D., Seidman, D. N., & Lavernia, E. J. (2013). Strengthening mechanisms in a high-strength bulk nanostructured Cu – Zn – Al alloy processed via cryomilling and spark plasma sintering q. *Acta Materialia*, *61*(8), 2769–2782. https://doi.org/10.1016/j.actamat.2012.09.036

[36] Yu, K. Y., Liu, Y., Sun, C., Wang, H., Shao, L., Fu, E. G., & Zhang, X. (2012). Radiation damage in helium ion irradiated nanocrystalline Fe. In *Journal of Nuclear Materials*. https://doi.org/10.1016/j.jnucmat.2011.10.052